Acta Cryst. (1999). A**55**, 274–288

Geometrical effects in diffraction analysis

N. Bernhoeft†

Institut Laue Langevin, 38042 Grenoble, France. E-mail: bern@drfmc.ceng.cea.fr

(*Received 17 December 1997; accepted 3 June 1998*)

Abstract

The use of X-ray and neutron scattering as a tool to study phase transitions is well established. As techniques improve and experiments are made under successively higher resolution, the need to consider the role of both the distribution of diffracting length scales and the incident-beam coherence volume is emphasized. The interplay of diffracting length scales and the beam coherence volume no longer permits calculation of diffraction profiles in terms of the sample intensity response convolved with an instrumental resolution function. Rather, the probe and sample now enter the calculation on an equal footing at the level of the scattering amplitudes. Under these conditions, it is found that the summation of coherent scattering amplitudes leads to characteristic profiles in wave-vector and, in the case of resonant X-ray scattering, energy space. In this latter case, in the vicinity of strong absorption edges, as used for example in resonant magnetic X-ray diffraction, the energy dependence of diffraction profiles may uniquely allow spatial localization of the scattering volume below the sample surface. This observation may considerably augment the range and power of resonant X-ray scattering.

1. Introduction

The use of scattering techniques as the pre-eminent tool to study, in microscopic detail, the mechanisms of a wide range of phase transitions is well established. The proportionality of the differential scattering cross section to a two-site correlation function has been formulated by van Hove (1954) and used as a basis for the interpretation of many experiments. In this paper, a discussion is given of the effects of incident-beam coherence and sample absorption on the interpretation of scattering experiments. It is found that, as the spatial resolution is increased, the increase in beam coherence volume plays a major role in the diffracted line shape. An underlying theme, general to the whole paper, is that under such conditions a calculation of the scattering intensity must treat the probe and sample together. In the proximity of a phase transition, or under conditions of strong absorption, the standard result that the measured intensity be given by a convolution of the sample intensity with a probe response function will be seen to break down.

The comments in §§2 and 3 on the interpretation of scattering intensity in terms of a two-site correlation function are general to any scattering process in which the probe–sample interaction may be reduced to this form. Normally this implies that the state function may be separated into two independent parts, namely that of the probe and that of the sample, *viz* the scattering process may be represented by a sufficiently weak interaction (pseudo-potential). The fundamental interactions are extensively discussed in the literature for both neutron and X-ray scattering (Marshall & Lovesey, 1971; Blume, 1985).

Possible geometric reasons for the observation of anomalous diffraction profiles are presented; for example, the common observation of a 'two-length-scale' profile in the disordered state in the vicinity of a phase transition, and the observation, in the ordered state, of split or multiple resonances in energy scans of resonant magnetic diffraction peaks. It is not claimed that these geometrical effects explain all of the bizarre observations in the literature, but simply that perhaps they deserve consideration before other conclusions are drawn. Since the problem of two-length-scale diffraction profiles in wave-vector space has recently been elegantly reviewed by Cowley (1996, and references therein), no detailed commentary on the experimental situation is included. On the other hand, the situation concerning the energy-dependent profiles, specific to resonant X-ray scattering, is less widely known and some brief experimental details are given.

To start, the term 'diffraction' as used here is defined. Experimentally, a diffractometer monitors the energy-integrated response at fixed scattering angle. For a probe of high incident energy compared with the relevant excitation spectrum of the sample, this yields a snapshot of the system (this point is amplified both in §2 and in Appendix *A*). In common with the kinematical and dynamical theories, the term diffraction will be used in the more restricted sense that the state of the sample be the same both before and after the scattering event. This implies that the sum over final states in the cross section is dominated by the term $|f\rangle = |i\rangle$ and has the advantage of permitting semi-classical calculations of intensities.

† Present address: Departement de Recherche Fundamentale sur la Matière Condensée, SPSMS, CEA/Grenoble, 17 rue des Martyrs, 38054 Grenoble CEDEX 9, France.

ISSN 0108-7673

The motivation for the use of such a 'single-state' approximation will be explained shortly. First, some important length scales in the problem are defined.

Length scale (1): The coherence length. For the probe, we consider the incident-particle/ray coherence volume. This has a longitudinal dimension, parallel to the propagation vector, which will be referred to simply as the 'coherence length', and two orthogonal transverse dimensions. At a wavelength λ, the magnitude of the coherence length is given by $\lambda^2/\Delta\lambda$. Associated with the (longitudinal) coherence length is a coherence time given by the coherence length divided by the incident particle speed.

Length scale (2): The correlation length. For the sample, we imagine, in the paramagnetic phase, the formation of islands of order on all length scales. The distribution is characterized by a correlation length. In the ordered state, the role of correlation length may be played by the domain size and in small samples by the relevant sample dimension, for example the thickness of a thin film.

Length scale (3): The absorption length. This length scale is dependent on the probe energy. While, on account of the low fluxes, resonances are generally avoided in neutron scattering experiments, techniques have been specifically developed to exploit the resonant dependence of X-ray scattering cross sections; for example, resonant magnetic X-ray diffraction and Templeton scattering.

The inverse of the probe coherence length sets a lower bound on the wave-vector resolution and, likewise, the probe coherence time sets a bound on the temporal changes in the sample-dependent properties. Thus, the initial state $|i\rangle$ of the sample will be considered 'frozen' and the single-state approximation $|i\rangle \rightarrow |i\rangle$ is useful in cases where the lifetime of $|i\rangle$ exceeds that of the probe coherence time. In the vicinity of a phase transition and in the ordered state, the lifetime of low-lying states may become extremely long and such an approach may be validated. The precise interval depends both on the probe coherence time and the sample correlation time; this results in sensitivity to the probe (neutron, X-ray), the incident monochromaticity and the state of the sample (for example, near-surface relaxation and defects may enhance the distribution of quasi-static modes).

Correspondences and differences are noted between this work and the conventional kinematical and dynamical theories of diffraction. All three approaches are rooted in the same single-state approximation enabling semi-classical calculation. The essential improvement of the dynamical theory lies in the self-consistent solution for the propagation of waves in a periodic lattice potential. As is well known, this gives rise to band gaps of forbidden frequencies of propagation, leading to the 'flat tops' of perfect crystal diffraction. A further aspect of the dynamical theory is beam attenuation by out-scattering, which leads to Lorentzian tails flanking the flat-top profile. In contrast, both the theory developed here and the kinematical picture correspond, from a quantum-scattering point of view, to a single (rather than multiple) collision of the photon (or neutron) with the crystal and exhibit neither band gaps nor out-scattering attenuation. It appears that, in principle, such effects may be included without difficulty in the present theory, although this has not yet been attempted. The present theory addresses the problem of partial beam coherence and its interplay with finite scattering volumes, which has been neglected in previous approaches.

The organization of the rest of the paper is as follows. §2 defines the terminology and experimental conditions, and the assumptions and approximations used in the analysis. A discussion of the role of primary-beam coherence and the interpretation of the scattering cross section is given; the more technical aspects are followed up in Appendices *A* and *B*. §3 deals with wave-vector-dependent profiles, ignoring the complication of absorption. It is demonstrated that a continuous distribution of regions of scattering density, over many length scales, may, under conditions of high spatial resolution, give rise to two component length-scale diffraction profiles. In the simulations, increasing the correlation length gives rise to reductions in the line widths of both components in the diffraction profile, which are found to collapse at different rates.

While the first two parts are general with respect to both neutron and X-ray scattering, §4 is devoted to the effect of absorption, which has been neglected in the earlier sections, and is particular to X-ray resonant scattering. For example, strong effects are anticipated at the uranium M_4, M_5 edges on account of their high absorption and the M_4 edge is treated in detail. It becomes necessary to consider the relative magnitudes of the three length scales: the absorption depth, the probe coherence length and the spatial extent of the scattering object. As in §3, only in certain limits is it possible to separate the observed intensity into idealized sample- and probe-independent parts. In general, a more careful calculation, treating the sample and probe on an equal footing, is required. Since this may open a way to measure the intrinsic energy line widths of the resonances, some experimental details are given. In addition, the important observation is made that, in favourable cases, a spatial localization of scattering below the sample surface may be made. This may considerably augment the diagnostic power of resonant (magnetic) X-ray scattering.

2. Coherence and resolution

Consider a scattering experiment. The incident beam is taken as a sum of independent rays; each ray within the beam has a coherence volume and coherence lifetime. If

the scattering process occurring within a given coherence volume cannot be localized, then the sum of all possible amplitudes must be taken in constructing the scattering probability. Scattering events occurring within two distinct coherence volumes may, by definition, be distinguished and their scattering probabilities summed to give the total scattering cross section from the incident beam. The summation of amplitudes within the (probe) coherence volume is what gives rise to, and limits the extent of, the measurement of the correlation function. The probe coherence volume then sets bounds on the resolution; the investigated spatial scale cannot be greater than the probe coherence volume and, likewise, the time scale of the correlations cannot be greater than the probe coherence time.† The appropriate correlation is measured subject to these bounds. At phase transitions, care must be taken not to be misled by size- and/or time-limited effects of the probe.

As an example, consider the measurement of the magnetic response function. When the spatial scale of magnetic order is greater than the probe coherence volume, the integrated intensity of scattered radiation is proportional to the square of the order parameter (within the classical two-site correlation model). However, close to the phase-transition temperature, often a region of great interest, islands of disorder will form within the ordered regions and one expects a wide distribution of length scales to be important in the problem (Wilson, 1979). The elemental scattering from a given ray is the coherent sum of scattering amplitudes over the distribution of length scales as it occurs within the given (probe) coherence volume. The total scattering is the sum of such elemental scattering intensities arising from the individual rays in the incident beam. This total scattering may differ in details from the standard prescription of the Fourier transform of a spatially averaged (thermodynamic) two-site correlation function. In the derivation of the cross section, one normally makes an implicit random phasing approximation [the extraction of a phase factor, $\exp(iqr)$, outside the matrix element]. Amplitude interference concerns fluctuations with lifetimes greater than, and length scales smaller than, those of the probe coherence volume (Appendices *A* and *B*). Care in interpretation may be necessary, for example, in the approach to magnetic order from the paramagnetic phase (Bernhoeft *et al.*, 1995; Stunault *et al.*, 1997).

The cross section is a sum of the scattering from individual coherence volumes weighted by an initial-state probability p_i. For this to represent an ensemble average implies that the typical probe coherence volume over which the summation is made is large enough to encompass a significant number of initial states (an argument for high incident-energy resolution and large incident coherence volume). However, if one is to perform an experiment as an ensemble average rather than a time average, the incident beam must contain many such volumes. A compromise is apparent between a trend towards very high incident resolution and the interpretation of results in terms of thermodynamic quantities.

The use of low-incident-energy particles (radiation) may pose a further problem of interpretation; in the concatenation of the scattering matrix elements (within the first Born approximation), to form the two-particle correlation function, one invokes the closure condition

$$\sum |\lambda_f\rangle\langle\lambda_f| = 1 \qquad (1)$$

in a sum over the final states. To ensure closure, this summation must involve the full interference of a complete set of states; if the final states are strongly filtered (within the first Born approximation the available final states are restricted by the energy of the incident particle), a suitable projection operator to limit the accessible states must be found to maintain closure and produce a correlation function. Limiting the accessible states may preclude straight-forward interpretation of the cross section in terms of a thermodynamic correlation function in some circumstances.

2.1. *A model system*

A simple cubic lattice is considered as a model system; the scattering plane is taken parallel to the plane containing the lattice vectors **a** and **c**. The sample has no miscut and is aligned with its surface normal, **c**, vertical, as in Fig. 1. The lattice sites are taken to have, unless otherwise stated, equal scattering power, which, to be 'concrete' is nominated the 'magnetic moment'.

3. Diffraction profiles as a function of scattered wave vector

In this section, scattering at fixed incident energy is considered, neglecting the effects of absorption, which are dealt with in §4 and Appendices *D* and *E*. The general conclusions will be appropriate for both neutron and X-ray (resonant and non-resonant) scattering. The variations arise only in the orders of magnitude of the characteristic length scales. As discussed in the *Intro-*

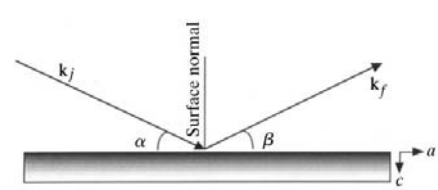

Fig. 1. The scattering geometry considered in the text.

† Intensity correlations, as opposed to scattering-amplitude corrections, may of course be measured on arbitrary long scales, as for example, in the study of Brownian motion by speckle experiments (Sutton *et al.*, 1991). Such higher-order correlation functions are not discussed here.

duction (§1), diffraction is considered where the integration over outgoing energies is sufficiently extensive that, to a good approximation, the instantaneous two-site correlation function is measured. Then, within the single-state approximation, the measured intensity from an elemental coherence volume is

$$I \propto |f|^2, \tag{2}$$

where

$$f = \sum_{z}^{N_z} \sum_{y}^{N_y} \sum_{x}^{N_x} m_{x,y,z} \exp[i(q_x r_x + q_y r_y + q_z r_z)]. \tag{3}$$

The sum has been split into orthogonal components N_x, N_y and N_z where there are N_x sites along the x axis *etc.* and one has $N = N_x\, N_y\, N_z$ sites within the probe coherence volume. For a scattering power m independent of site index,

$$I \propto m^2 \frac{\sin^2(q_x N_x a/2)}{\sin^2(q_x a/2)} \frac{\sin^2(q_y N_y a/2)}{\sin^2(q_y a/2)} \frac{\sin^2(q_z N_z a/2)}{\sin^2(q_z a/2)}. \tag{4}$$

This yields a peak intensity of order m^2N^2 with a peak width, along each q_i, of order $1/N_i a$. Absorbing an inessential factor of $1/a^3$ into the constant of proportionality, this gives an integrated intensity proportional to m^2N per coherence volume. In an illuminated sample volume V there will be V/Na^3 coherence volumes, yielding a final integrated intensity proportional to m^2V, as expected.

Expanding the intensity within the given coherence volume along a given component of the scattered wave vector, *e.g.* q_z, one obtains, for small q_z,

$$\begin{aligned} I(q_z, N_z) &\propto \frac{N_z^2[1 - (N_z^2 q_z^2 a^2/2^2 3!)\ldots]^2}{[1 - (q_z^2 a^2/2^2 3!)\ldots]^2} \\ &= \frac{N_z^2}{\{1 + [(N_z^2 - 1) q_z^2 a^2/2^2 3!]\}^2} \\ &= \frac{N_z^2}{[1 + (q_z^2/\Gamma^2)]^2}, \end{aligned} \tag{5}$$

a Lorentzian squared function with half width inversely proportional to the number of coherent scattering planes. At larger scattering angles, the envelope of successive maxima of $\sin^2(N_z q_z a/2)$ will fall as $1/q_z^2$, giving rise to Lorentzian-like tails. This, the scattering from an elemental volume, thus has a tendency towards a diffraction profile with a sharp central peak superposed on a broader tail.†

Consider what happens now upon addition of such terms as each elemental volume contributes to the scattering power. One may identify two distinct cases. In case (1), the existence of long-range order, the scattering power of the sample is uniform over the incident-radiation coherence length. In case (2), short-range order, there exists a distribution of magnetization correlation lengths within a typical probe coherence length. It may be noted that in this context the definition of long- or short-range order depends not only on the sample but also on the probe characteristics. Explicitly, the maximum value of the summation in equation (4), N_z, nominated $N_{\max}$, is different in the two instances. In case (1), $N_{\max}$ is given by the probe coherence length, while in case (2) $N_{\max}$ is given by the intrinsic correlations in the sample.

3.1. *Case (1)*

In the first case, the distribution of probe coherence lengths in the incident beam will result in the total scattered intensity being a summation of the form

$$I_{\text{total}}(q) = \sum_{N_{\text{coh}}} \Re(N_{\text{coh}}) I(q, N_{\text{coh}}), \tag{6}$$

where to be explicit we have written $N_{\max} = N_{\text{coh}}$ and where $I(N_{\text{coh}})$ is the elemental scattering intensity from each incident coherent radiation volume taken up to the limit of the individual ray. $\Re(N_{\text{coh}})$ is the probability distribution function of the coherence lengths of the rays in the incident beam. Since the peak intensity and line width are both non-linear functions of N_{coh}, the distribution $\Re(N_{\text{coh}})$ can alter the diffraction profile.

3.2. *Case (2)*

The second case may be separated into two parts, (2.i) and (2.ii). In (2.i), taking $\Re(N_{\text{coh}})$ to be the same for all rays, *i.e.* a δ function at a given probe coherence length N_{coh}, we consider the case where each ray has within it a single ordered region of size N_{sample}, smaller than N_{coh}. Thus, $N_{\max}$ for a given ray is determined by the sample distribution N_{sample}. Different rays will in general encompass ordered regions of different sizes. This would correspond to an image of a material approaching a magnetic phase transition where the regions of instantaneous order are 'dilute' on the scale of N_{coh}. This gives

$$I_{\text{total}}(q) = \sum_{N_{\text{sample}}} P(N_{\text{sample}}) I(q, N_{\text{sample}}), \tag{7}$$

where $P(N_{\text{sample}})$ is the intrinsic distribution of correlation lengths and $I(q, N_{\text{sample}})$ is the corresponding intensity distribution.

In (2.ii), the individual rays enclose more than one region of order within their bounds, and the regions of order within the given coherence volume may be of different sizes. This is difficult to treat in any general manner; a model distribution of the local order must be given (see for example the discussion in Appendix *B*).

The distinction between cases (1) and (2.i) is that in the latter the bound arises from the sample while in the former it is a property of the probe. Despite their

† The tendency to Lorentzian tails is enhanced by the effects of absorption, as in §4.

different origins, mathematically they give the same summations and thus case (1) will be considered in the treatment of (2.i). The difference between (2.i) and (2.ii) is that in the former an incoherent sum of intensities has to be performed and in the latter a coherent sum over the ordered regions within the individual coherence volume has to be performed first. In an experiment, one may have to consider the convolution of both effects.

3.3. *Numerical results*

Diffraction profiles from a typical correlation-length distribution function are considered. Since the summations over x, y, z are independent, attention will be focused on the results of scattering along one direction, hereafter nominated q. It should be noted however, that, unless rather special precautions are taken, there is a cross-coupling between the scattering in specular and off-specular directions, *i.e.* q_z and q_x, q_y, through the resolution function. In this work, since they are inessential to the argument and to avoid clouding the discussion, angular resolution effects are ignored at all levels (see Appendix *C*).

In the following example, we note that the same sample distribution $P(N_{\text{sample}})$ of scattering objects gives rise to a single Lorentzian profile for a low (probe) coherence length, and to the appearance of a two-length-scale diffraction profile when examined with a high probe coherence length (high spatial resolution).

A model distribution function, $P(N_{\text{sample}})$, along an axis z is chosen with the form $(1/z)\exp(-z/\zeta a)$, where ζ is the correlation length in lattice units (a). The motivation for the choice of this form is its similarity to the Ornstein–Zernike form for the static susceptibility which is measured in the instantaneous approximation. In practice, the precise form is not critical to the arguments that follow. In this example, the length scale, ζ, acts as a convenient parameter in the model. Case (2.i) is assumed, that is, each probe coherence volume has one scattering region within it. The scattering observed is then proportional to the following sum where each term represents the scattered intensity from a region of dimension Na encompassed by an individual ray,

$$\sum_{1}^{N_{\text{coh}}} \frac{1}{Na} \exp\left(\frac{-N}{\zeta}\right) \frac{\sin^2(Nqa/2)}{\sin^2(qa/2)}. \tag{8}$$

This sum has been numerically investigated by varying the values of correlation length (ζ) and for two different values of probe coherence volumes (N_{coh}). In the first study, N_{coh} is given the value 100 lattice units to represent an experiment under conditions of low resolution, while, in a second set of simulations, it was set equal to 1000 lattice units to represent a high-resolution experiment. For both calculations, the step in q was taken to be 0.001 r.l.u. (reciprocal-lattice unit).

3.4. *Low-resolution study ($N_{coh} = 100$)*

First, it is found that, if the correlation length is small (typically less than 40 lattice units), the profile of intensity against the modules of the wave vector (q) may be well approximated by a single Lorentzian. The fitted Lorentzian half-width at half-maximum (HWHM) scales with the inverse correlation length in this regime. In Fig. 2(b), a calculated diffraction profile at a value of sample correlation length $\zeta = 15$ is presented together with a Lorentzian fit. As ζ increases, the profile sharpens and remains approximately Lorentzian; however, the HWHM is now found to decrease less quickly than ζ^{-1} on account of the limit to the observable correlations imposed by the probe coherence volume N_{coh}. This is the spatial resolution limit.

Since this model system is to be a crude representation of the behaviour in the vicinity of a phase transition, the intrinsic correlation length ζ as a function of a variable t is considered, where $t = (T - T_c)/T_c$ represents a (hypothetical) reduced temperature. This then permits one to investigate the characteristics of the intensity profiles as a function of t, as summarized in Table 1 and Fig. 3.

At low correlation lengths, the variation of the HWHM, $\Gamma_{\text{Lorentzian}}$, is determined by the imposed

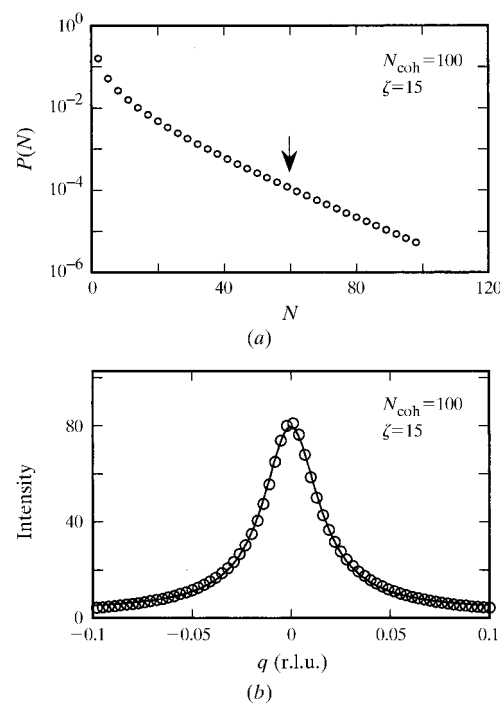

Fig. 2. (a) The probability distribution on a logarithmic scale used in the calculation of the scattering profile [case (2.i)] for a correlation length, ζ, of 15 lattice units and a probe coherence length of 100 lattice units. The inverse of the HWHM is approximately 3.7 to 4 times greater than ζ, as illustrated by the vertical arrow. In (b), the points give the result of the numerical simulation and the solid line through the points is a fit to a single Lorentzian function.

Table 1. *Characteristics of the intensity profiles of the low-resolution study*

$N_{coh} = 100$	$\zeta < 50$
ζ imposed as power of t	-1.0
Line shape	Lorentzian
HWHM as power of t	0.8 (1)
Intensity at $q = 0$ as power of t	-1.5 (1)

behaviour of ζ. In the same regime, the intensity of the scattering at $q = 0$ increases somewhat faster than the correlation length. Once the effect of probe coherence-length limiting comes into play, neither the behaviour of the Lorentzian HWHM nor its intensity follow simple power laws for an imposed power-law behaviour of ζ.

3.5. *High-resolution study ($N_{coh} = 1000$)*

In simulations for $N_{coh} = 1000$ lattice units, the behaviour is, as expected on the basis of the above observations, straightforward at low correlation lengths. The simulation is dominated by the behaviour of $P(N_{sample})$. One has a single Lorentzian line shape with a HWHM increasing inversely with ζ. The effect of spatial resolution is illustrated in Fig. 4 for the case where $\zeta = 50$ and the calculated diffraction profiles are given for incident beams of both low and high resolution with $N_{coh} = 100$ and 1000, respectively. As anticipated, the low-q portion for $N_{coh} = 1000$ is more intense, giving rise to a narrower half width.

At higher values of ζ, a new feature appears, namely a two-component line shape. In Fig. 5, simulations for the cases $\zeta = 10$ and 100 lattice spacings are presented. The lower plot ($\zeta = 10$) retains the simple Lorentzian form, while the upper plot ($\zeta = 100$) is dominated by a sharp central peak riding on a broader feature. The two components in this latter plot may be approximately analysed in terms of the sum of a Lorentzian and a Lorentzian-squared line shape, this is shown by the solid line. In the two-component line shape, the narrow Lorentzian-squared term takes over the dominant central region and the Lorentzian is now the broader, and weaker, component. Perhaps it should be stressed that no new length scales have been introduced to the distribution. The observed effect arises from the increased spatial resolution of the probe. The results are summarized in Table 2 and illustrated in Fig. 6.

3.6. *Summary of behaviour*

The above comment on the role of the probe coherence volume in diffraction profiles is not an answer to the two-length-scale problem. It may, however, be worth emphasizing that, under high resolution, if the physical length scale ζ varies for some reason as t^{-1} (*e.g.* Altarelli *et al.*, 1995), then there may appear a 'broad' component which varies approximately in the manner expected for thermodynamic fluctuations (see Cowley, 1996, and references therein). This could be

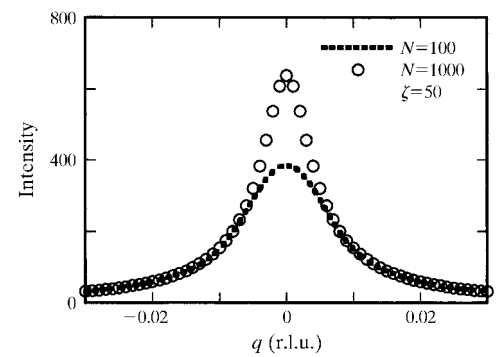

Fig. 4. The calculated scattering profiles at fixed sample correlation length, ζ = 50, and for two different values of probe coherence length. For wave vectors above 0.01 r.l.u. the calculated points lie upon one another; at low q the increased spatial resolution available for N = 1000 allows the peak to develop. Both profiles are essentially Lorentzian; however, at high resolution the HWHM is reduced by approximately 40%.

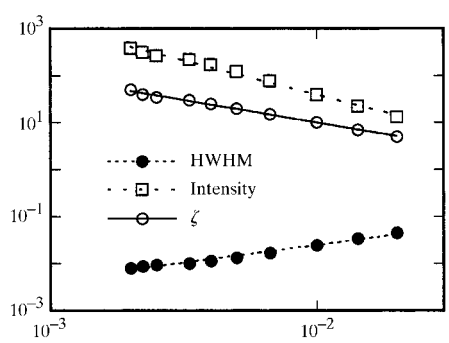

Fig. 3. For an imposed variation of ζ on the variable t (reduced temperature), the figure gives the corresponding variations in HWHM and intensity at q = 0 resulting from Lorentzian fits to the numerical simulations. The probe coherence length is 100 lattice units. For ζ varying as t^{-1}, the HWHM is found to be proportional to $t^{0.8}$ and the intensity to $t^{-1.5}$.

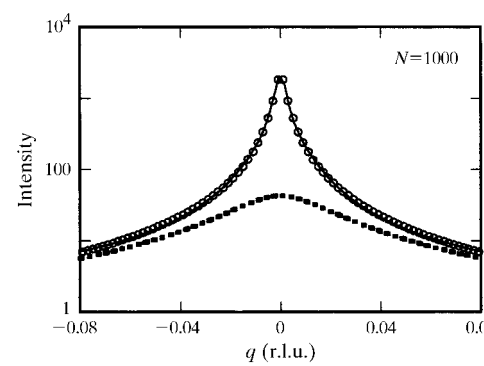

Fig. 5. The lower plot shows the simulation for ζ = 10 and the upper for ζ = 100, at N_{coh} = 1000. The single Lorentzian line shape at low ζ is replaced by a more sharply peaked function, which may be approximately represented by the sum of a Lorentzian and a Lorentzian-squared function (full line through the points in upper plot).

Table 2. *Characteristics of the intensity profiles of the high-resolution study*

$N_{coh} = 1000$	$\zeta < 50$	$50 < \zeta < 200$
ζ imposed as power of t	−1.0	−1.0
Line shape	Lorentzian	Lorentzian plus Lorentzian squared
HWHM as power of t	0.8 (1)	0.60 (4) + 0.85 (8)
Intensity $q = 0$ as power of t	−1.5 (1)	−1.26 (6) + −1.9 (1)

misleading. In the analysis of a full experiment, one would also have to take into account the angular resolution, probe coherence volume distribution [case (1)], and the interference arising from scattering regions located within a given probe coherence volume [case (2.ii)]. Finally, the effects of absorption,† spatial variation of defect density (*e.g.* near-surface roughness) and, where relevant, domain formation and variation of magnetization within the sample volume, may play more significant roles in a given observation (Bernhoeft *et al.*, 1995; Stunault *et al.*, 1997). What is clear, however, is that there is a tendency for the diffraction profile to have a 'two-component' form when looked at in sufficient detail. This effect is superposed on the distribution $P(N_{sample})$ and it may be difficult to disentangle the two.

4. Energy-dependent diffraction profiles (X-rays)

The problem of absorption is now considered; in particular, the effects of the strong energy dependence of absorption encountered in X-ray resonant diffraction. It will be shown that exploitation of resonant-energy-dependent diffraction profiles may allow X-rays uniquely to spatially localize the source of scattering below the sample surface. To the author's knowledge, previous use has not been made of this effect. The effects of absorption will also, in the appropriate limits, play a role in the discussion given in §3 above, where they lead to Lorentzian tails in the wave-vector-dependent diffraction profiles. In this work, for ease of discussion, the wave-vector and energy dependencies of the scattering profiles are considered separately. In experimental analysis, one must consider both together as necessary.

4.1. *The model*

We consider again the model system introduced in §2. As mentioned in the *Introduction* (§1), there are three principal length scales to consider. First, the probe coherence length. For simplicity, as in the discussion of case (2.i), the distribution function $\Re(N_{probe})$ is approximated by a δ function at N_{coh}. Second, there is the depth from the sample surface below which the sample exhibits a scattering power. For example, in the case of a thin film of uniform magnetization, the scattering power may be more or less abruptly terminated by the substrate. Or, in a large sample, in the vicinity of a phase transition one may have the phenomenon of near-surface ordering (disordering) in the presence of bulk disorder (order) (Stunault *et al.*, 1997).‡ Third, there is the absorption depth. This quantity may be strongly energy dependent in the vicinity of an absorption edge, *e.g.* in resonant (magnetic) scattering.

4.2. *Scattering from a uniform sample*

Uniform sample scattering power as a function of depth is assumed. In the case that the longitudinal probe coherence length is much smaller than the absorption depth, *i.e.* the normal case of low absorption, one may correct diffraction profiles, as a function of incident energy, neglecting the role of coherence (see Appendix *D* where this standard calculation is repeated for completeness). More subtle effects occur when the absorption depth and probe coherence lengths are similar. In this case, one has to take account of the change in scattering power occurring within the coherence volume.

Focusing attention on the variation of the diffraction profile with incident energy at the Bragg point of the scan (all scattering elements in phase), for a simple resonant process with a Lorentzian (in energy) line shape, one gets

$$I \propto \frac{\Gamma^2}{\Gamma^2 + (\Delta E - \hbar\omega)^2} \left\{ \frac{m[1 - \exp(-\mu^* N_{max} a)]}{[1 - \exp(-\mu^* a)]} \right\}^2, \quad (9)$$

where, for a beam incident at angle α and exiting at angle β,

$$\mu^* = (\mu/2)(1/\sin\alpha + 1/\sin\beta). \quad (10)$$

Equation (9) splits naturally into two parts, both dependent on the incident photon energy. In the first factor, Γ is the effective inverse lifetime of the scattering process, ΔE the energy step between the initial and intermediate states of the resonant process, and $\hbar\omega$ the incident photon energy. In the second part, m is the site magnetic moment, μ the energy-dependent inverse absorption length [*viz* the intensity falls as $\exp(-\mu L)$ over a distance L], N the number of lattice sites in the

† It is of interest that the exponentional decay of beam intensity with path length gives an identical form (with opposite sign) to the profile as obtained by considering a rough surface with an exponentially depleting number of layers (Stunault *et al.*, 1997). The two effects may work one against the other to yield spurious estimates of both surface roughness and absorption coefficients.

‡ Parenthetically, it is noted that effective non-uniform scattering power for diffraction in a given direction may also arise from, for example, a depth-dependent distribution of magnetic domain sizes. This distribution, for example large surface domains to small bulk domains, will alter the coherent scattering power as a function of depth, mimicking a changing magnetic moment. Careful analysis of the wave-vector-dependent profiles in orthogonal directions may be used to resolve this case.

coherent sum, and a the lattice parameter. The extension by which the formula becomes a function also of the scattered wave vector is given in Appendix *E*.

One readily sees, in the limit of negligible absorption with μa and $\mu a N_{\max}$ both small, that the second factor in (9) will scale like $m^2 N^2_{\max}$ and one has an analysis as in §3. Considering, in this section, the profile in energy at fixed scattered wave vector, one sees that, in this limit, it is independent of μ and hence will be a simple Lorentzian of half width Γ. This is distinct from the case, calculated in Appendix *D*, where the absorption is weak on the scale of the probe coherence length but important on the scale of the total diffracting thickness. Finally, in the limit that μa is small but $\mu a N_{\max}$ is large, *i.e.* the scattering from a material in which the absorption gives important changes in scattering power over the longitudinal probe coherence length, one obtains an intensity

$$I \propto \frac{\Gamma^2}{\Gamma^2 + (\Delta E - \hbar\omega)^2} \left[\frac{m}{\mu^* a}\right]^2. \qquad (11)$$

This profile is characteristically broadened, or split, on account of the incident-energy dependence of μ.

The discussion just given, for scattering from a diffracting volume starting at the sample surface, will be modified for those incident rays which are not scattered within the first coherence length. They will make a contribution that is $\exp(-2\mu^* a N_{\rm coh})$ weaker. By assumption, this attenuation is large and their contribution has been neglected in the calculations described below. These corrections are set out in the latter part of Appendix *D*.

In the calculation of relative angular intensities of different Bragg reflections, one also has to take care of the angular dependence of the incident-beam footprint, Lorentz factor and the geometrical factors in the cross section. We note that, in comparison with the standard formula [equation (34) in Appendix *D*], an extra angular dependence is implied in the case of strong absorption on account of the factor μ^{*2} in the denominator (as opposed to μ). This may be important when (semi-) quantitative use is made of resonant intensities.

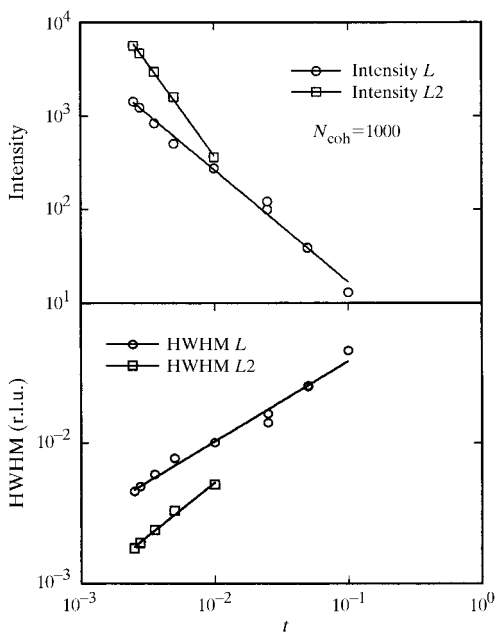

Fig. 6. For a given variation of ζ with the parameter t, $\zeta \propto t^{-1}$, the plots show the dependence widths and intensities of the fitted sum, Lorentzian (L) plus Lorentzian-squared ($L2$) profiles. The model parameters for $N_{\rm coh}$ and ζ have typical experimental values of 1000 and 20 to 200 lattice spacings, respectively. The upper panel gives the variation of intensity at q = 0 while the lower gives the corresponding dependence of HWHM on t. Approximate power-law behaviour is found, as given in Table 2.

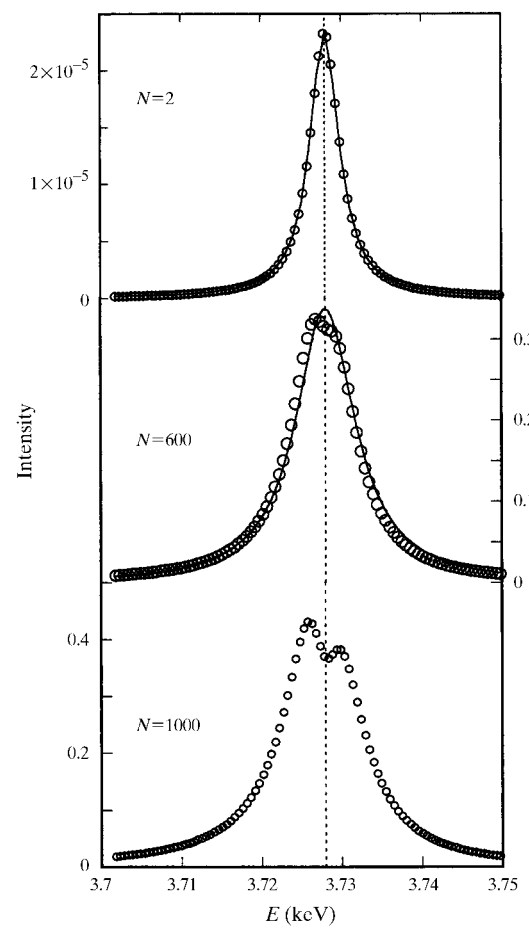

Fig. 7. Simulations at the Bragg point of the energy profiles for scans through the M_4 uranium absorption edge. From top to bottom, 2, 600 and 1000 correlated lattice planes are diffracting, respectively. The parameters used are given in Appendix *F*. For less than 600 planes, the profile remains approximately Lorentzian, as illustrated by the solid lines in the upper two plots. The dotted line marks the position of the maximum of the absorption profile at 3.728 keV [equation (41)].

4.3. *Example: uranium M_4 resonance*

By way of example, the energy dependence at a (magnetic) Bragg peak has been calculated in the strong absorption limit. That is to say, at each incident energy, one sets the crystal to the Bragg condition in q-space and monitors the intensity as a function of incident photon energy. For the numerical calculation, the (001/2) Bragg reflection is chosen with a c-axis parameter of 4 Å, using equation (9), for the case of uranium M_4 resonance. A parameteric form of the M_4-edge absorption, as measured in transmission from UO_2 thin films (Cross *et al.*, 1998), has been used in the calculations. This, along with other numerical parameters, is discussed in Appendix *F*.

The results of the calculations are shown as the points in Fig. 7; the solid lines are least-squares fits to the approximate Lorentzian profile, an approximation that becomes successively poorer as the number of diffracting layers increases. At the top of the figure, for few diffracting layers (low $N_{\max}$), the profile in energy is close to Lorentzian and the HWHM is close to the input value $\Gamma = 2.2$ eV. On increasing $N_{\max}$, a broadening and splitting commence although the peak maintains an approximately Lorentzian form, as shown in the central frame of Fig. 7, until, at the bottom of Fig. 7, two peaks have formed, the low-energy peak being characteristically the higher on account of the increased absorption occurring above the resonant edge.

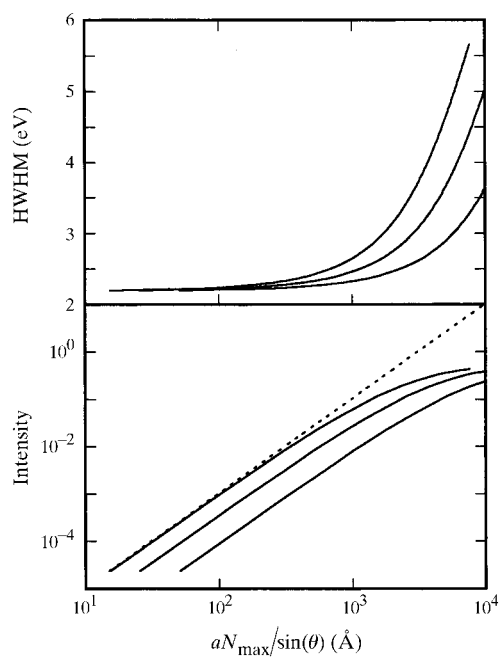

Fig. 8. The variation of (Lorentzian) HWHM in energy for Bragg scattering at the M_4 uranium resonance, and its intensity at the resonant energy are shown in the upper and lower frames, respectively. The calculations have been made for three different uranium densities: 10, 6 and 3 g cm^{-3} going from the upper to the lower curves. The parameters for the simulations are given in Appendix *F*.

The condition of peak splitting depends on the relative values of $N_{\max}$ and the absorption length. $N_{\max}$ may be controlled either by varying the incident-beam coherence length or the number of diffracting layers (*e.g.* by use of thin films or exploiting the temperature-dependent correlation lengths in a sample near the point of the phase transition). The absorption length may be varied with the concentration of uranium nuclei. Assuming that the absorption of the uranium ion is independent of its local environment in a given set of materials, one may follow the evolution of the HWHM with both $N_{\max}$ and absorption length. In the top frame of Fig. 8, from top to bottom, curves of the resonant profile half-width for uranium densities of 10, 6 and 3 g cm^{-3} are given. For values of HWHM less than about 4 eV, the predicted peak splitting is not marked and, in the presence of instrumental energy resolution, may go undetected. The intensity of the response at the resonant energy, as modelled by a Lorentzian fit, is displayed in the bottom frame of Fig. 8. In addition, for the highest uranium density, a dotted line has been added to show the $N_{\max}^2$ dependence that would be anticipated in a more elementary approach [equation (3)]. One sees that, for large optical path lengths, a short fall in intensity may amount to almost an order of magnitude in this most extreme case. This could lead to, for example, erroneous estimates of the evolution of the order parameter in a material where the domain size changes with temperature.

4.4. *Scattering from a thin film*

Since the use of energy-dependent scattering is less well established in the literature, and on account of the fundamental interest in the measurement of resonant-energy line widths, a method to measure intrinsic magnetic resonant widths in the presence of strong absorption is proposed. The method is to prepare the material in the form of a thin film. The experiment consists of measuring the resonant-energy profile for a series of specular reflections and determining the film thickness either by reflectivity or by some external means (deposition rate, mass *etc.*). In a given Bragg event, the depth of magnetic reflection is limited by the physical film thickness, this then allows one to calculate the energy-dependent profile from which Γ may be estimated.† Such experiments have recently been carried out (Bernhoeft *et al.*, 1998).

4.5. *Scattering from a non-uniform sample*

A restricted number of diffracting magnetic layers may also arise in materials that show near-surface

† Given the absorption of the resonant species as a function of energy determined, for example, from the intensities of the substrate peaks or by transmission or fluorescence.

ordering. In such materials, in the vicinity of the phase transition, one may have a magnetic surface layer only a few tens of an ångström thick. The energy-dependent diffraction profile may be used to establish the fact that this layer *is* in the near surface and, furthermore, one may monitor its evolution with temperature. This spatial localization of the diffraction volume is unique to such strongly absorbing processes and extends the range of information available in resonant scattering experiments. The intensity of diffraction of such regions appears, experimentally, at least in some cases, to be related to the near-surface condition. A close study of this effect may help to shed some light on the physical origin of the occurrence of two-length-scale diffraction profiles in scans against wave vector (Bernhoeft *et al.*, 1998).

The case of materials that show a depression of magnetization near the surface is also interesting. In this case, the presence of 'dead' layers, which diffract only weakly, if at all, allows the strongly energy-dependent absorption to alter considerably the diffraction profile in energy. It may give rise to the formation of a 'pair' of peaks at the resonance; the exact details become sensitive to the assumed magnetic configuration. Examples are given in Fig. 9; it is seen that ten layers do not much affect the profile, while 50 layers (200 Å) leave their mark. Such dead layers may arise due to surface damage (250 layers in the model given corresponds to 0.1 μm, a not untypical depth of damage), the presence of non-diffracting domains preferentially forming at the near surface, or a non-magnetic layer, due perhaps to oxidation.

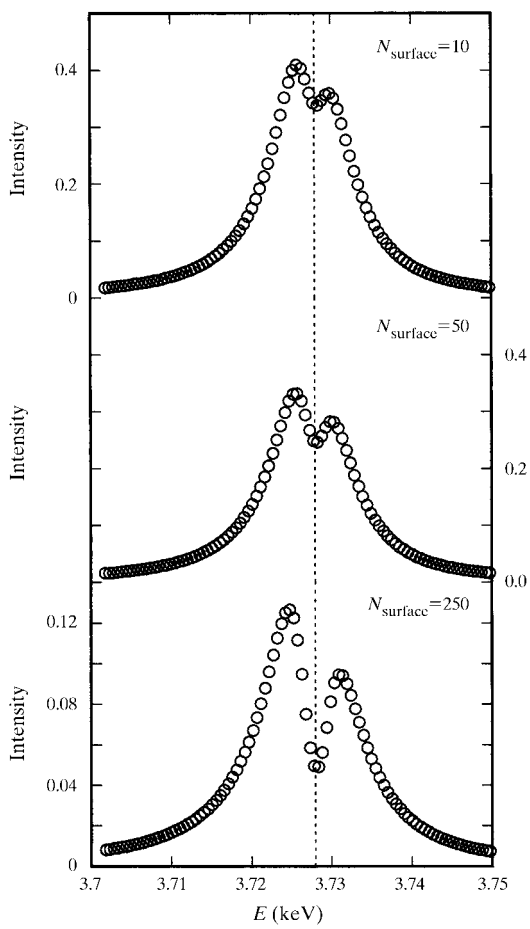

Fig. 9. In the presence of 'dead' surface layers, the energy-dependent profiles of Bragg scattering at the M_4 uranium edge show a variety of structures. From the top to the bottom, the number of non-diffracting layers increases from 10 to 50 to 250 for a constant total depth of diffraction of 1000 layers. The remaining parameters and the dotted vertical line are as in Fig. 7.

5. Conclusions

The roles of geometric effects, the incident-beam coherence volume and the sample-dependent absorption and distribution of scattering power have been discussed. Their interplay may give rise to interesting effects in both wave-vector and energy scans; in particular, when the partial coherence of the incident beam is significant the analysis of diffraction profiles in terms of a sample response function convolved with an instrumental resolution function may fail.

For a given distribution function, it is shown in §3 that (i) the wave-vector profile under conditions of low spatial resolution is Lorentzian in form, and (ii) under conditions of higher spatial resolution one obtains a profile which evolves from a single Lorentzian form to one better described as the sum of a Lorentzian plus a Lorentzian-squared profile as the sample correlation length, ζ, is increased. Further, if ζ varies with a model parameter t, taken to represent the reduced temperature, as $\zeta \propto t^{-1}$, then, under the conditions of high resolution, the apparent temperature dependence of the HWHM of the Lorentzian component may mimic that of thermodynamic fluctuations, while the Lorentzian-squared component has a more rapidly decreasing line width. This illustrates that (i) the observation of a two-component profile may be possible in a system that has a single representative length scale, and (ii) the approximate power-law dependencies of the widths and intensities of the two components may be misleading.

In §4, energy analysis at a resonant-diffraction profile is discussed. It is found that, unique to this technique, spatial localization of the diffracting volume may be possible, allowing diffraction experiments, rather than grazing-incidence surface scattering, to be performed with the ability to localize spatially the source of the scattering. This observation considerably augments the diagnostic power of resonant X-ray scattering.†

† *Noted added in proof:* Since submitting this article, a publication on the role of partial coherence in scattering has appeared (Sinha *et al.*, 1998).

APPENDIX *A*

In the conventional analysis, the scattering probability can, aside from a set of constants related to the system–probe interaction, be represented in the following form (Marshall & Lovesey, 1971):

$$S(q,\omega) = \int_{-\infty}^{\infty} \frac{\mathrm{d}t}{2\pi\hbar}\, \exp(-i\omega t) \sum_i p_i \times \left\langle i \left| \sum_j \exp[-iqR_j] \sum_k \exp[iqR_k(t)] \right| i \right\rangle, \quad (12)$$

where $\hbar\omega$ is the difference between the outgoing and incident energy of the probe. One sees that the instantaneous correlation is not encumbered by time asymmetrization. This limit is reached by equal integration over all outgoing energies

$$\int \mathrm{d}\omega\, S(q,\omega) = \int_{-\infty}^{\infty} \frac{\mathrm{d}t}{2\pi\hbar}\, \delta(t) \sum_i p_i \times \left\langle i \left| \sum_j \exp[-iqR_j] \sum_k \exp[iqR_k(t)] \right| i \right\rangle \quad (13)$$

and allows one to write the scattering probability in the form

$$S(q) = \sum_{i,f} p_i \left| \left\langle f \left| \sum_j \exp[-iqR_j] \right| i \right\rangle \right|^2. \quad (14)$$

In the (semi-classical) calculations of the main text, designed to highlight the role of coherence in diffraction profiles, the sum over all states $|f\rangle$ is approximated by the (supposed dominant) self term $|i\rangle$. The state $|i\rangle$ is labelled by $N_{\max}$ appropriate to the coherence volume of a given ray.

By contrast, the scattering falling into a small band of frequencies at ω_0 is given by integration with the filter function $\delta(\omega - \omega_0)$ yielding, as is well known, the Fourier component at ω_0:

$$\int \mathrm{d}\omega\, \delta(\omega - \omega_0) S(q,\omega) = \int_{-\infty}^{\infty} \frac{\mathrm{d}t}{2\pi\hbar} \exp[-i\omega_0 t] \sum_i p_i \times \left\langle i \left| \sum_j \exp[-iqR_j] \sum_k \exp[iqR_k(t)] \right| i \right\rangle. \quad (15)$$

In particular, the zero frequency, or elastic response, is seen to be the equal integration over all time of the t-asymmetric correlation function

$$S(q,0) = \int_{-\infty}^{\infty} \frac{\mathrm{d}t}{2\pi\hbar} \sum_i p_i \times \left\langle i \left| \sum_j \exp[-iqR_j] \sum_k \exp[iqR_k(t)] \right| i \right\rangle. \quad (16)$$

Note that in the case of strong absorption the probe wavefunction will decay within the coherence volume, giving rise to a complex scattering wave vector. This gives rise not only to Lorentzian tails in wave-vector scans, as discussed by Bernhoeft *et al.* (1995) and Stunault *et al.* (1997) (beam depletion by out-scattering is likewise the physical origin of the Darwin tails in perfect-crystal diffraction) but also interesting effects in energy scans through an energy resonance as discussed in §4.

APPENDIX *B*

The distinction between the straight Fourier transform of a two-site correlation function that is dependent only on the sample and the analysis given may be described as follows. First, it is recognised that the (total) cross section is a weighted sum over probe coherence volumes of matrix elements evaluated within a probe coherence volume; this is the content of equation (12). Continuing as in, for example, equation 3.12 of Marshall & Lovesey (1971), one introduces a random phasing approximation and extracts a phase factor $\exp(iqr)$ outside the matrix element. The matrix elements so formed are then averaged over coherence volumes and finally (spatially) Fourier transformed according to the extracted phase factor $\exp(iqr)$.

In contrast, if the phased sums are made within a coherence volume, yielding a harmonic function of argument (qaN), then these act as the appropriate set of transform functions on the distribution $p_i(N)$ [equation (14)]. In case (2.i) (§3.2), the transform functions are $\sin^2(qaN/2)/\sin^2(qa/2)$ [equation (8)] and it is these transform functions that give rise to the tendency to form a sharp peak at the zone centre superposed on a broad background. In the situation where there are many accessible final states, *i.e.* beyond the single-state approximation, the sum over final configurations will tend to wash out the domineering contribution of the high-N states to the transform functions, $\sin^2(qaN/2)/\sin^2(qa/2)$. This lowers the spatial resolution. The role of time averaging is to introduce a random phasing within the matrix elements. Recall that the phenomenon of time averaging is limited by the probe coherence time. If the different states cannot be accessed within this time, for example on account of critical slowing down or lifetime enhancement due to the presence of local defects, disorder, surface *etc.*, then a quasi-frozen distribution will be seen and the final

states will be strongly restricted and one may arrive at the single-state approximation. This suggests that curious wave-vector diffraction profiles may be enhanced by probes with good q resolution and poor incident-energy resolution (relative to the lifetime of the fluctuations). Case (2.ii) (§3.2) has, in general, more intricate transform functions, which have to be determined in each case. They will tend to retain the same peaking structure on account of being coherent sums. Finally, in §4, the absorption within a coherence volume is introduced. This yields a complex, as opposed to harmonic, transform. The transform functions are given for the simplest case in Appendix E [equation (39)].

In the final part of this Appendix, it is noted that simple analytic forms may be given for certain distributions $P(N_{\text{sample}})$. In particular, the normalized top-hat distribution for correlation lengths between N_0 and N lattice spacings,

$$P_{\text{sample}} = \frac{1}{N+1-N_0}, \tag{17}$$

yields a profile

$$I_{\text{total}}(q) = \frac{1}{2\sin^2(qa/2)}\left\{1 - \frac{\cos[qa(N+N_0)/2]}{N+1-N_0} \times \frac{\sin[qa(N+1-N_0)/2]}{\sin(qa/2)}\right\} \tag{18}$$

and the normalized triangular distribution for $m = 1$ to N,

$$P_{\text{sample}}(m) = \frac{m}{N(N+1)/2}, \tag{19}$$

yields

$$I_{\text{total}}(q) = \frac{1}{2\sin^2(qa/2)}\left\{1 - \frac{\sin[qa(2N+1)/2]}{(N+1)\sin(qa/2)} + \frac{\sin^2(qaN/2)}{N(N+1)\sin^2(qa/2)}\right\}. \tag{20}$$

These distributions maybe useful as blocks with which to build more complex functions P_{sample}. It should be noted that, depending on the instrumental angular resolution both within and out of the scattering plane, one may have to consider an effective distribution for P_{sample} taking into account the integration, or lack of integration, in the two orthogonal directions to that of the scan variable [see discussion in §3 around equation (4)]. In particular, if the scattering objects are approximately isotropic in space, and the spectrometer does not provide sufficient integration in the orthogonal directions under conditions of high resolution, the larger scattering objects will gain rapidly in scattering power over the smaller ones, tending to augment the effective tail at large N_{corr} in P_{sample}. This will increase the relative importance of the sharp component, leading to more pronounced temperature dependencies. In a similar way, in frequency space, the role of probe coherence time and integration over outgoing energies may influence the effective P_{sample}.

APPENDIX *C*

In the main text, the incident energy resolution is approximately taken into account by the finite (longitudinal) coherence length of the probe, while the smearing of wave-vector profiles due to the angular resolution is suppressed. The angular or spatial resolution has two parts. First, there is the angular distribution of (probability amplitude) paths to be summed over within a given coherence volume, and, second, there is the angular spread of the rays (due to focusing optics *etc.*), which leads to a summation of intensities weighted by an appropriate angular (distribution) function. The former, at the level of transition amplitudes, has to be included within the coherent summation and expresses the spatial (transverse) extent of the incident coherence volume Ξ.

$$I_{\text{ray}} \propto \left| \sum_j \int_{\Xi} D_f(\beta - \beta_0) f(\mathbf{Q}, \mathbf{r}_j) D_i(\alpha - \alpha_0)\, \mathrm{d}\alpha\, \mathrm{d}\beta \right|^2, \tag{21}$$

where $D_{i,f}$ is the distribution of the (indistinguishable) paths that have to be included in the summation over Ξ and $\mathbf{Q}$ is the scattered wave vector. In the text, we set $D_i(\alpha - \alpha_0) = \delta(\alpha - \alpha_0)$, and likewise for D_f, that is, the smearing within the coherence volume is suppressed in order that the results should be as simple as possible.

The finite monochromaticity of the incident beam has an additional effect, not taken into account by the restricted summation over the coherence volume, owing to the dependence of the magnitude Q on the magnitude k_i. This may be included by an integration over the appropriate distribution $A(k_i - k_0)$ within the coherence volume,

$$I_{\text{ray}} \propto \left| \sum_j \int_{\Xi} A(k_i - k_0) f[\mathbf{Q}(k_i), \mathbf{r}_j]\, \mathrm{d}k_i \right|^2, \tag{22}$$

where the implicit dependence of Q on k_i is made explicit. Energy filtering of scattered radiation is taken into account at the level of intensities in the normal manner. Likewise, the angular distribution of the incident and scattered rays then needs to be taken into account *via* an angular resolution function $R(\alpha, \beta)$ operating on the intensities. $R(\alpha, \beta)$ is equivalently expressed as a function of the scattered wave vector in the paragraph below.

Following the nomenclature of Fig. 1, an expression is derived for the experimental resolution function in the (q_x, q_z) coordinate system in terms of the angular variables α and β and their deviations $\delta\alpha, \delta\beta$. Three

principal components are associated with the spectrometer: the monochromaticity of the incident X-ray beam, the finite divergence of the incident beam upon the sample, and the finite acceptance angle of the detector. It is assumed that the incoming and outgoing angular deviations are uncorrelated and that there is no energy selection of the scattered photons over the energy range of interest (few eV at a typical energy of several keV). The sample contributes to the resolution principally through its mosaic spread and possibly by its finite size for a small incident beam. Taking the incident monochromaticity, angular divergence and sample mosaic together, an effective incident angular divergence $\delta\alpha$ is defined in the vertical plane. In the same plane, for open detector slits at a distance l from the sample and an illuminated sample of length s, we have an outgoing divergence approximately given by $\delta\beta = \{\delta\alpha^2 + [(s/l)\sin\beta]^2\}^{1/2}$. For an incident beam of height w smaller than the sample length, s is to be replaced by $w/\sin\alpha$. α and β are assumed to be distributed about their mean values in Gaussian fashion, yielding an angular resolution function

$$R(\alpha, \beta) = N \exp[-(\delta\alpha/\alpha)^2] \exp[-(\delta\beta/\beta)^2] \tag{23}$$

with a normalization

$$N = (\pi\delta\alpha\delta\beta)^{-1} \tag{24}$$

for the case where the slits are sufficiently wide open not to cut the outgoing beam. On transformation to the (q_x, q_z) coordinate system,

$$R(\delta q_z, \delta q_y) = NJ \exp(-A_{xx}) \exp(-B_{zz}) \exp(-C_{xz}) \tag{25}$$

with

$$A_{xx} = [\cos^2\beta/(\delta\alpha)^2 + \cos^2\alpha/(\delta\beta)^2][\delta q_x/(k_0 \sin 2\Theta)]^2 \tag{26}$$

$$B_{zz} = [\sin^2\beta/(\delta\alpha)^2 + \sin^2\alpha/(\delta\beta)^2][\delta q_z/(k_0 \sin 2\Theta)]^2 \tag{27}$$

$$C_{xz} = [-2\sin\beta\cos\beta/(\delta\alpha)^2 + 2\sin\alpha\cos\alpha/(\delta\beta)^2] \times [\delta q_x/(k_0 \sin 2\Theta)][\delta q_z/(k_0 \sin 2\Theta)] \tag{28}$$

$$J = [k_0^2 \sin(\alpha + \beta)]^{-1} \tag{29}$$

$$2\Theta = \alpha + \beta. \tag{30}$$

APPENDIX *D*

The calculation of absorption corrections when the absorption over one coherence length is weak, and yet the total sample absorption is important, proceeds by summation of intensities from each coherence volume. This is in contrast to the case of strong absorption where a summation of amplitudes within the coherence volume must be made. First, the standard calculation for the intensity or scattering from a uniform object is made in two, equivalent, manners. We start with a continuum approximation: for an incident beam of intensity I_0 at an angle α, the intensity per unit area, from a thickness dz of sample located at depth z is

$$dI = I_0 \exp(-2\mu^* z) \frac{d\sigma}{d\Omega} \frac{dz}{\sin\alpha}, \tag{31}$$

where the full beam is intercepted by the sample and the effect of its footprint is made explicit. The cross section per unit volume is $d\sigma/d\Omega$ and the absorption coefficient is defined as

$$\mu^* = \frac{\mu}{2}\left(\frac{1}{\sin\alpha} + \frac{1}{\sin\beta}\right) \tag{32}$$

for a beam incident at angle α and exiting at angle β. The implicit assumption is that the scattered intensity is proportional to the illuminated volume even as this volume is taken to the infinitesimal dz. This gives, for scattering from depth z,

$$I(z) = \frac{I_0[1 - \exp(-2\mu^* z)]}{2\mu^* \sin\alpha} \frac{d\sigma}{d\Omega}, \tag{33}$$

which enables corrections to be made by direct multiplication. In the case of specular reflection from a body of large dimensions, the expression simplifies to a total intensity per unit area

$$I = \frac{I_0}{4\mu} \frac{d\sigma}{d\Omega}. \tag{34}$$

The energy-dependent correction factor of $1/\mu$ is to be compared with the correction $1/\mu^2$ in the case of strong absorption [equation (11)]. In the specific case of the uranium M_4-edge treated in the main text, a calculation, parallel to that given in §4, for this weak absorption limit yields a Lorentzian line shape of HWHM = 4.4 eV, in comparison with the two-peaked structure in the bottom frame of Fig. 7.

An alternative derivation, which highlights the nature of the approximations, may be made in terms of the scattering from individual coherence volumes. Since by assumption the absorption per coherence volume is weak, the diffracted intensity from a given coherence volume is proportional to $\exp(-2\mu^* Na)$, where Na is the absorbing depth contained in a coherence volume. The total intensity per unit area is the sum over the length of r coherence volumes along the incident-beam direction,

$$I = \frac{I_0}{\sin\alpha} \frac{d\sigma}{d\Omega} Na\left[\sum_r \exp(-2\mu^* Nar)\right]. \tag{35}$$

Here the factor Na arises from the diffracted intensity of an elemental coherence volume [see discussion under equation (4) in §3]. For a semi-infinite body in specular reflection, one has, as above,

$$I = \frac{I_0}{4\mu}\frac{\mathrm{d}\sigma}{\mathrm{d}\Omega}. \tag{36}$$

Finally, the formula for the total intensity per unit area is written as the sum over the length of r coherence volumes along the incident-beam direction in the case of strong absorption. Following the notation in the main text,

$$I \propto \frac{\Gamma^2}{\Gamma^2 + (\Delta E - \hbar\omega)^2}\left[\frac{m[1-\exp(-\mu^* N_{\max} a)]}{[1-\exp(-\mu^* a)]}\right]^2 \times \left[\sum_r \exp(-2\mu^* N_{\max} a r)\right], \tag{37}$$

which, for a semi-infinite body, interpolates between the limits of strong and weak absorption as

$$I \propto \frac{\Gamma^2}{\Gamma^2 + (\Delta E - \hbar\omega)^2}\left[\frac{m[1-\exp(-\mu^* N_{\max} a)]}{[1-\exp(-\mu^* a)]}\right]^2 \times \frac{1}{[1-\exp(-2\mu^* N_{\max} a)]} \tag{38}$$

uncorrected for footprint or Lorentz factor.

APPENDIX *E*

The scattering from a set of N consecutive objects in a given coherence volume with absorption coefficient μ is given by

$$I \propto [1+\exp(-2\mu^* Na) - \exp(-\mu^* Na)2\cos(qNa)] \times [1+\exp(-2\mu^* a) - \exp(-\mu^* a)2\cos(qa)]^{-1}, \tag{39}$$

where the Lorentzian energy resonant pre-factor has been suppressed for clarity and q is the reduced wave vector from the Bragg point. This may be readily extended to deal with the case of more than one scattering species (Stunault *et al.*, 1997). In the appropriate limits, it reduces to the formulae given in the main text (§§3, 4).

When $\mu^* a$ is small, corresponding to negligible absorption over one lattice parameter, and in the region where $\cos(qa)$ is close to 1, the formula simplifies to

$$I \propto [1+\exp(-2\mu^* Na) - \exp(-\mu^* Na)2\cos(qNa)] \times [\mu^{*2} + q^2]^{-1}. \tag{40}$$

In the limit that $\mu^* Na$ is dominant, suppressing all dependence on wave vector in the numerator, one has a Lorentzian line shape in q at a given photon energy. Thus, the wave-vector width may, in this limit, become dependent on μ^* and independent of N. Given sufficient spatial resolution, this may yield a method to extract $\mu(E)$ from the incident-energy dependence of the wave-vector line width of the diffraction profile.

APPENDIX *F*

The data for the parameterization of the absorption coefficient of the M_4 uranium resonance were obtained by transmission through films of UO_2 (Cross *et al.*, 1998). The data show a very weak oscillation above the absorption edge which is not captured by our simple parametric form. The coefficient, in Å^{-1}, over the experimental range is

$$\mu_{M_4} = 10^{-4}\{1.25 + 0.16\,\mathrm{invtan}[(\hbar\omega - \Delta E)/\Gamma] + 3.5\Gamma^2/[\Gamma^2 + (\hbar\omega - \Delta E)^2]\}, \tag{41}$$

where the invtan is calculated in radians, the energies are in keV with $\Delta E = 3.728$, $\Gamma = 0.0022$, and $\hbar\omega$ is the incident photon energy. For completeness, a corresponding value for the M_5 edge is

$$\mu_{M_5} = 10^{-4}\{0.8 + 0.16\,\mathrm{invtan}[(\hbar\omega - \Delta E)/\Gamma] + 7.5\Gamma^2/[\Gamma^2 + (\hbar\omega - \Delta E)^2]\} \tag{42}$$

with parameters $\Delta E = 3.552$ and $\Gamma = 0.0020$.

In the calculations shown in the main text, Γ and ΔE of the resonance [equations (10) and (12)] were set equal to their values at the M_4-absorption edge.

I wish to thank my colleagues for their advice and criticism. In particular, I thank Christian Vettier for introducing me the field of magnetic X-ray scattering, his open advice and constant support. I thank Anne Stunault and Gerry Lander for critical reading of the manuscript. Some of this work was performed while I held a HCM Grant from the EEC, and partial support from the Institut for Transuranium Elements Karlsruhe is acknowledged. I thank the directors and staff of ILL Grenoble for their generous support over the past years.

References

Altarelli, M., Nunez-Regueiro, M. D. & Papoular, M. (1995). *Phys. Rev. Lett.* **74**, 3840–3843.

Bernhoeft, N., Heiss, A., Longridge, S., Stunault, A., Wermeille, D., Vettier, C., Lander, G. H., Huth, M., Jourdan, M. & Adrian, H. (1998). *Phys. Rev. Lett.* **81**, 3419–3422.

Bernhoeft, N., Stunault, A., Vettier, C., de Bergevin, F., Gibbs, D., Thurston, T. R., Shapiro, S. M., Hastings, J. B., Dalmas, P., Helgesen, G. & Vogt, O. (1995). *J. Magn. Magn. Mater.* **140–144**, 1421–1422.

Blume, M. (1985). *J. Appl. Phys.* **57**, 3615–3618.

Cowley, R. A. (1996). *Phys. Scr.* T**66**, 24–30.

Cross, J. O., Newville, M., Rehr, J. J., Sorensen, L. B., Bouldin, C. E., Watson, G., Gouder, T., Lander, G. H. & Bell, M. I. (1998). *Phys. Rev. B*, **58**, 11215–11225.

Hove, L. van (1954). *Phys. Rev.* **95**, 249–262.
Marshall, W. & Lovesey, S. W. (1971). *Theory of Thermal Neutron Scattering*. Oxford University Press.
Sinha, S. K., Tolan, M. & Gibaud, A. (1998). *Phys. Rev. B*, **57**, 2740–2758.
Stunault, A., Langridge, S., Vettier, C., Gibbs, D. & Bernhoeft, N. (1997). *Phys. Rev. B*, **55**, 423–438.
Sutton, M., Mochrie, S. G. J., Greytak, T., Nagler, S. E., Berman, L. E., Held, G. A. & Stephenson, G. B. (1991). *Nature (London)*, **352**, 608–609.
Wilson, K. G. (1979). *Sci. Am.* **241**, 140–157.